Title
Gentle topography increases vertical transport of coarse dust by orders of magnitude

Journal
Journal of Geophysical Research: Atmospheres, 126(14)

ISSN
2169-897X 2169-8996

Authors
Heisel, Michael
Chen, Bicheng
Kok, Jasper F
et al.

Publication Date
2021-07-21

DOI
10.1029/2021JD034564

Data Availability
The data associated with this publication are available at: https://doi.org/10.5068/D15Q4C

Peer reviewed

JGR Atmospheres

RESEARCH ARTICLE
10.1029/2021JD034564

Gentle Topography Increases Vertical Transport of Coarse Dust by Orders of Magnitude

Michael Heisel[1], Bicheng Chen[2], Jasper F. Kok[1], and Marcelo Chamecki[1]

[1]Department of Atmospheric & Oceanic Sciences, University of California in Los Angeles, Los Angeles, CA, USA, [2]Department of Civil & Environmental Engineering, University of California in Berkeley, Berkeley, CA, USA

Key Points:

- Hill topography increases the likelihood of coarse dust particles (60 micrometer diameter) reaching high elevation by orders of magnitude
- The hill induces three transport mechanisms: upslope flow, ejection from the crest, and dispersion in the highly turbulent wake
- Global dust models, which underestimate coarse dust concentrations, can be improved by including a parameterization of topography effects

Supporting Information:

Supporting Information may be found in the online version of this article.

Correspondence to:

M. Chamecki,
chamecki@ucla.edu

Citation:

Heisel, M., Chen, B., Kok, J. F., & Chamecki, M. (2021). Gentle topography increases vertical transport of coarse dust by orders of magnitude. *Journal of Geophysical Research: Atmospheres*, *126*, e2021JD034564. https://doi.org/10.1029/2021JD034564

Received 8 JAN 2021
Accepted 28 JUN 2021

Abstract The presence of coarse mineral dust in the atmosphere has been substantiated in several recent measurement campaigns, which include observations of particles up to and above 100 μm in diameter. Yet, atmospheric dust models either do not include particles larger than 20 μm or severely underestimate their concentrations. One possibility for the underestimated concentrations is that models do not represent enhancements of particle transport due to subgrid-scale topography. Here, large-eddy simulations are used in combination with Lagrangian particle tracking to assess the impact of gentle two-dimensional topography with 50 and 100 m elevation on the vertical transport of coarse dust in neutrally stratified conditions. The presence of topography significantly increases the likelihood that 5 and 20 μm particles reach several hundred meters in altitude. Further, topography increases this likelihood by orders of magnitude for larger 60 μm particles. Three mechanisms are observed to contribute to the increased vertical transport: a strong upward mean flow region on the uphill side of the topography, ejection of particles downwind of the topography crest, and enhanced vertical dispersion in the wake of the crest. The compounding effects of these mechanisms provide a pathway for coarse dust emitted from the surface to reach elevations where they can be further transported into the free atmosphere by large-scale motions such as convective plumes. While these findings are motivated by mineral dust observations, they are generally applicable to other heavy aerosols such as pollen.

1. Introduction

Dust particles emitted in the atmosphere are responsible for numerous phenomena of global consequence here on Earth. In particular, coarse dust (with diameter greater than 5 μm) absorbs shortwave and longwave radiation which contributes to warming of the planet (Kok et al., 2017), redistributes mineral nutrients such as iron and phosphates to ocean (Jickells et al., 2014) and land ecosystems (Swap et al., 1992) through its long-range transport, and alters the nucleation of clouds and their subsequent precipitation (Mahowald & Kiehl, 2003).

Given the importance of coarse dust to local and global processes, it is critical for models to accurately represent coarse dust concentrations. Yet there is a consistent disparity between measured observations and global dust models, where models severely underestimate the presence of coarse dust (Adebiyi & Kok, 2020; Kok, 2011; Rosenberg et al., 2014; Ryder et al., 2019). This model inaccuracy has been demonstrated through measurement campaigns (Betzer et al., 1988, and references therein), which in recent years have predominantly focused on Saharan dust (Denjean et al., 2016; Jung et al., 2013; Rosenberg et al., 2014; Ryder et al., 2018). Some of these campaigns identified dust particles up to and above 100 μm in diameter at altitudes between 60 and 5,000 m (Rosenberg et al., 2014; Ryder et al., 2018). Particles in this size range are often referred to as "giant" dust, and the long-range transport of giant dust remains a mystery (van der Does et al., 2018). In contrast, many global models do not include particles larger than 20 μm (Huneeus et al., 2011; Mahowald et al., 2014; Wu et al., 2020).

As noted above, models that do incorporate coarser dust tend to substantially underestimate its concentration (e.g., Adebiyi & Kok, 2020; Ansmann et al., 2017; Sodemann et al., 2015). This likely occurs in part because of underestimations in both the coarse dust lifetime (Huang et al., 2020; Maring et al., 2003; van der Does et al., 2018; Weinzierl et al., 2017; Yu et al., 2019) and the fraction of emitted dust mass that is coarse (Huang et al., 2021; Kok et al., 2021). A factor contributing to these underestimates may be that models miss or underresolve relevant dynamics. The entrainment (emission) of particles from the surface

into the atmosphere is commonly parameterized by the surface shear stress in excess of a threshold (Ginoux et al., 2001; Kok et al., 2012; Zender et al., 2003). Following emission, the particle fate is determined by near-surface turbulent winds which may lift the particle to higher altitudes or deposit it. For global simulations with grid size typically on the order of tens of kilometers, near-surface turbulence and a multitude of related small-scale processes are either coarsely parameterized or neglected.

One such underresolved process is the response of the wind to topographical features smaller than the model grid. While some models parameterize the enhancement of roughness and drag due to topography (see, e.g., Beljaars et al., 2004; Jiménez & Dudhia, 2012), the complex mean and turbulent flow patterns around the topography are not accounted for in models. Rosenberg et al. (2014) measured enhanced fluxes of coarse dust in the presence of topography, and suggested the upflow and flow separation around the topography may be responsible for the enhancement. For flat topography, dust particles larger than 20 μm are predominantly concentrated within the first few meters above the surface (Freire et al., 2016), which is perhaps the justification for neglecting coarser dust in many models. The possibility that topography induces coarse dust transport well above traditional predictions is consistent with recent studies that demonstrated even gentle topography such as hills or ridges can strongly modulate the transport of scalar gases (Chen et al., 2019, 2020; Katul et al., 2006; Ross, 2011).

The present study extends upon these passive scalar transport studies to evaluate the effect of topography on coarse dust particles. The impetus for the study is to identify the intermediate mechanisms bridging the initial entrainment of dust particles near the ground to their eventual transport into the upper atmosphere by large-scale motions such as convective plumes (Freire et al., 2016; Lindau et al., 2021; Klose & Shao, 2013). The ultimate goal is to improve global dust models by providing insight into the near-surface wind dynamics which both enhance the uplift of coarse dust and are missing from current dust models.

To this end, the present investigation comprises large-eddy simulations (LES) of flat topography and two hill sizes, where each simulation is coupled with a Lagrangian tracking routine to infer particle behavior. Three coarse particle sizes—5, 20, and 60 μm diameter—are tested for each of the three LES topography cases, thus totaling nine scenarios. The LES and Lagrangian tracking are further described in Section 2. The study results are then given in Section 3, followed by concluding remarks and a discussion of the results in the context of global dust models in Section 4. Finally, the LES topography results are validated using a reference test case presented in Appendix A.

2. Methods

2.1. Flow Simulations

2.1.1. Numerical Modeling

In the LES approach, the flow velocity on a three-dimensional numerical grid is evolved using filtered versions of the governing Navier-Stokes and mass conservation equations (Deardorff, 1970). For the present case of an implicit filter, the simulation can only resolve the dynamics of motions larger than twice the grid spacing, owing to Nyquist's sampling theorem. The evolved flow velocity, which directly reflects these resolved motions, is hereon referred to as the "LES resolved" velocity. The effect of any smaller motions, in particular the dissipative scales for which viscosity is important, must be represented by a subgrid-scale (SGS) model.

The LES solver in the present study uses an in-house pseudo-spectral code on a staggered vertical grid (see, e.g., Albertson & Parlange, 1999). Spatial derivatives are computed in Fourier space for the horizontal directions x and y, while a second-order-accurate central difference scheme is utilized for the vertical direction z. Periodic boundary conditions are employed in x and y where the spectral approach is used. The flow is evolved in time using a second-order-accurate Adams-Bashforth integration scheme. The SGS model employed here parameterizes the small-scale fluid stresses using the Smagorinsky-Lilly formulation (Lilly, 1966; Smagorinsky, 1963), whose coefficient is continuously updated using a scale-dependent Lagrangian dynamic model (Bou-Zeid et al., 2005).

Rather than customizing the numerical grid to conform to the topography surface, an immersed boundary method is used to represent the topography within the cartesian grid (Mittal & Iaccarino, 2005). Specifically,

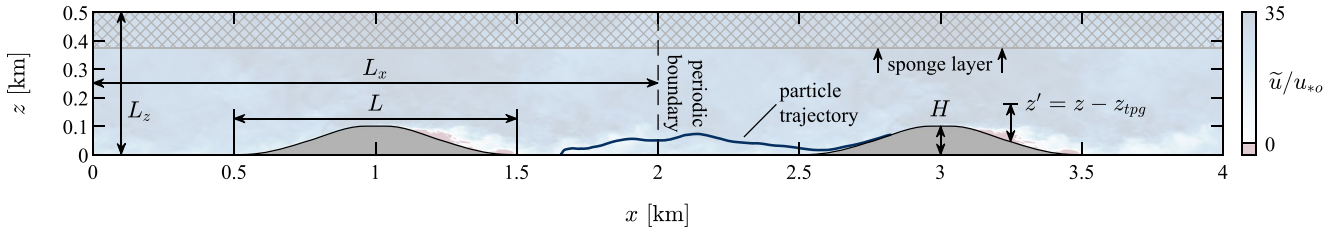

Figure 1. The large-eddy simulation (LES) domain setup demonstrating the domain size (L_x, L_z) with periodic boundaries in x (and y, not shown), hill dimensions (H, L), height relative to the hill elevation (z'), and an example tracked particle trajectory. The hatched area indicates the sponge layer of the domain. An instantaneous LES resolved velocity field $\tilde{u}(x, z)$ for the large hill case is shown in the background. The negative velocity color is exaggerated to highlight the presence of flow separation and recirculation for this case.

an external force is applied to grid points inside the immersed boundary to ensure a zero-velocity condition in this region. The surface shear stress is estimated using an equilibrium wall model based on the log law at the grid points neighboring the immersed boundary. Further details on the present immersed boundary treatment are provided in Chester et al. (2007). The combination of the sharp velocity difference across the immersed boundary (in the horizontal direction) and the use of Fourier transforms in the spectral code result in unphysical oscillations known as Gibbs phenomenon. This effect is mitigated here by smoothing velocities inside the boundary with cubic interpolation prior to spectral calculations in the solver (Li et al., 2016). The immersed boundary treatment is validated in Appendix A, where results from the present code are shown to match reasonably well with a reference test case (Gloerfelt & Cinnella, 2019).

2.1.2. Setup

The simulated flow scenarios are simplified here to reduce the number of competing effects and isolate the influence of topography. Most notably, the present simulations neglect Coriolis forces and are limited to a neutrally stratified boundary layer with no influence by temperature and buoyancy effects. The role of convection and the coupling of topography and buoyancy effects is reserved for a future study.

The three LES topography cases are designed to explore the different regimes with respect to flow separation: a flat surface with no topography (i.e., the control case), a relatively shallow hill where no flow separation occurs, and a steeper hill exhibiting flow separation and a recirculation region. For simplicity, two-dimensional hills with height $z_{tpg}(x)$ invariant in y are considered here. The hill shape, shown in Figure 1, is approximately the inverse of a fourth-order polynomial (Hunt & Snyder, 1980). The same shape has been used extensively in both physical and numerical experiments (Breuer et al., 2009; Frölich et al., 2005; Kähler et al., 2016; Rapp & Manhart, 2011, among many others), thus providing a well-documented case to validate the LES and ensure accurate results.

The hill parameters are listed in Table 1. The case names "small" and "large" hill refer to the hill heights relative to each other. To achieve a more realistic topography, the aspect ratio between the hill height H and overall length L is reduced from 1:4 in previous studies to 1:10 here in the steeper case. While the hill height H = 50 and 100 m is varied, the length L = 1,000 m is fixed. Based on the prescribed surface roughness, hill length, and maximum hill slopes, the presence of a separation region (or lack thereof) for the hill cases is consistent with theoretical predictions (Wood, 1995). The aerodynamic roughness length z_o = 0.003 m is based on typical values for Northern Africa (Stull, 1988).

The hill is located in the longitudinal center of the domain with length L_x = 2,000 m, width L_y = 1,000 m, and depth L_z = 500 m. Because the domain is periodic in x as depicted in Figure 1, the topography is effectively a series of hills rather than a single isolated hill. The same domain dimensions are used for the flat case. The top 25% of the domain is a sponge layer, where velocity fluctuations are increasingly damped as the upper boundary is approached in order to enforce the stress-free boundary condition. The simulations are designed to accurately model the lowest 200–300 m of a neutrally stratified boundary layer, which is the altitude region most relevant to the goal of the study. The sponge layer helps to reduce the impact of the upper boundary on the lower portion of the domain, and later results do not present statistics within the sponge layer above z = 375 m.

Table 1
Large-Eddy Simulation (LES) Parameters for the Three Topography Cases

Variable	Symbol	Topography case		
		Flat	Small hill	Large hill
Hill length (m)	L	0	1,000	1,000
Hill height (m)	H	0	50	100
Maximum hill slope (deg.)	θ_{max}	0	9.8	19.0
Upstream wind speed (m/s)	$U(x$ =0 m, z =500 m)	11.5	11.6	11.4
Surface roughness (m)	z_o		0.003	
Duration (min)	T		40	
Domain size (grid points)	$N_x \times N_y \times N_z$		320 × 160 × 160	
Domain size (m)	$L_x \times L_y \times L_z$		2,000 × 1,000 × 500	
Grid resolution (m)	$\Delta x \times \Delta y \times \Delta z$		6.25 × 6.25 × 3.125	

The mean flow conditions are dictated by the prescribed pressure gradient forcing in the longitudinal direction. The forcing for each case was adjusted to achieve a matched "upstream" mean wind speed at the position farthest from the hill, that is, $U(x = 0\text{m}, z = 500\text{m}) \approx 11.5$ m/s. The mean wind speed at this position is assumed to be negligibly affected by the hill presence, and thus can be used to infer the wind conditions upstream of the hill. Based on the log-law mean wind profile and the roughness z_o, this wind speed corresponds to shear velocity $u_{*,o} = u_*(x = 0\text{m}) = 0.37$ m/s. Matching the upstream wind speed and shear velocity ensures the incoming flow conditions are approximately the same across cases. Differences in the wind speed and surface stress along the hill, such as local increases in shear velocity $u_*(x)$, are then solely due to the topography. The velocity $u_{*,o}$ also corresponds to the average surface stress at every position in the flat case, and is used as the primary scaling velocity in the later results. For reference, the velocity at $z = 10$ m in the flat case is 7.75 m/s (17.3 mph), corresponding to strong wind conditions.

2.2. Lagrangian Particle Tracking

2.2.1. Numerical Modeling

Instantaneous fields (i.e., in x, y, z, and time t) of the LES resolved velocities and SGS stresses were stored for the Lagrangian particle tracking to be performed separately from the LES. The particle trajectories are estimated by integrating the following equation:

$$\frac{d\mathbf{x}_p}{dt} = \mathbf{u_p}, \tag{1}$$

where $\mathbf{x}_p$ is the particle position, $\mathbf{u}_p$ is the particle velocity, and bold typeface indicates a three-component vector. The particle velocity is not necessarily in equilibrium with the flow velocity, owing to the inertial response of the particle to flow accelerations both in the mean wind around the topography and turbulent fluctuations. An additional relation is required to account for the particle acceleration in response to the flow:

$$\frac{d\mathbf{u}_p}{dt} = \frac{\Delta\mathbf{u}}{t_p} + \mathbf{g}, \tag{2}$$

which is a simplified force balance comprised of drag and gravitational acceleration (e.g., Sawford & Guest, 1991). The gravitational term $\mathbf{g} = (0,0,-g)$ acts only in the vertical direction in this system. The acceleration in Equation 2 is integrated using a Verlet scheme to estimate $\mathbf{u}_p$, and thereafter a second-order Adams-Bashforth scheme is employed for Equation 1 to update the particle position.

Table 2
Parameters for the Three Particle Sizes

Variable	Symbol	Particle case		
		5 μm	20 μm	60 μm
Density (kg/m^3)	ρ_p		2.65	
Diameter (μm)	D_p	5	20	60
Relaxation time (s)	t_p	0.00020	0.0032	0.025
Terminal settling speed (m/s)	W_s	0.0020	0.031	0.25
Normalized settling (−)	W_s / u_{*_o}	0.0054	0.086	0.68
Reynolds number (−)	Re_p	0.00067	0.043	1.0

The drag term in Equation 2 is based on the difference $\Delta\mathbf{u} = \tilde{\mathbf{u}} + \mathbf{u}_{sgs} - \mathbf{u}_p$ between the flow and particle velocity, where $\tilde{\mathbf{u}}$ is the LES resolved velocity and $\mathbf{u}_{sgs}$ is the modeled subgrid-scale velocity. The velocities are evaluated at the current particle position $\mathbf{x}_p$, and interpolation of the LES grid is used to estimate the velocities at the exact particle position. In this study, the SGS velocity is modeled stochastically using a Langevin equation (Weil et al., 2004). Following Weil et al. (2004), the flow autocorrelation time is used as the relevant time scale for integrating the Langevin equation. However, to ensure this time scale represents the inertial particle trajectory rather than the flow trajectory, the time scale is updated using the particle velocity and the correction formula in Sawford and Guest (1991). The time scale correction is also discussed elsewhere (see, e.g., Comola et al., 2019; Wilson, 2000). The scheme of Bailey (2017) is used to improve numerical stability when integrating the Langevin equation. Finally, the SGS turbulent kinetic energy inputted to the stochastic equation is estimated from the model of Mason and Callen (1986).

The drag term also depends on the particle relaxation time

$$t_p = \frac{\rho_p D_p^2}{18\,\mu\left(1 + 0.15 Re_p^{0.687}\right)} \tag{3}$$

based on Stokes' Law and the particle density ρ_p, particle diameter D_p, and air viscosity μ. Equation 3 includes a correction based on the particle Reynolds number $Re_p = \rho \mid \Delta\mathbf{u} \mid D_p / \mu$, where ρ is the air density (Clift et al., 2005). The correction is required to better represent the effect of turbulence on the drag, which is non-negligible for $Re_p \gtrsim O(1)$.

The equilibrium condition for Equation 2, that is, $d\mathbf{u}_p / dt = 0$, is achieved when $\Delta\mathbf{u}$ reaches the terminal settling speed $W_s = t_p g$. If it is assumed that the particles are always in equilibrium, which is valid if t_p is much smaller than the flow time scales, then $\mathbf{u_p}$ is simply the flow velocity minus the settling W_s. Throughout most of the domain, t_p is less than 1% of the average flow autocorrelation time scale. To test the influence of inertial accelerations on vertical transport, we tracked 60 μm particles for one topography case using two methods: The first method solved for $\mathbf{u}_p$ using Equation 2 and a Verlet scheme as described above, and the second employed $\mathbf{u}_p = \tilde{\mathbf{u}} + \mathbf{u}_{sgs} - W_s$ which satisfies the equilibrium condition and assumes the particles are inertialess. There is less than 10% difference between the two methods for all statistics presented later, such that assuming inertialess particles does not affect the conclusions of the study. This test indicates gravitational settling is more important than inertial accelerations for the vertical transport of coarse dust in the presence of topography. However, Equation 2 and inertial accelerations are included in the analysis for completeness.

The immersed boundary and Lagrangian particle codes described above were previously used in studies of canopy turbulence (Chen et al., 2019, 2020), and the inclusion of inertial effects follows Comola et al. (2019). The particle parameters for this study are listed in Table 2, noting the density is based on silica dust. While the particles are not always settling at the terminal speed, W_s is used here as the characteristic velocity for gravitational settling. The listed particle Reynolds numbers are based on this velocity W_s.

Lastly, mineral dust is known to exhibit a range of complex, non-spherical shapes (Kandler et al, 2007) which require a correction to the drag coefficient (Hölzer & Sommerfeld, 2008; Huang et al, 2020). The focus here is general trends across a range of particle sizes and topography rather than any effects of shape variability on the drag and settling. Accordingly, Equation 3 assumes spherical dust particles for simplicity.

2.2.2. Setup

To begin each particle trajectory, the particle is given a random initial position in x and y, with a starting height one meter above the topography surface (i.e., $z' = 1$ m). The choice to introduce particles at random horizontal positions is favored over explicitly modeling dust emission from the surface due to limitations in the wall-modeled LES. Throughout most of the LES domain, the majority of turbulent motions are directly

resolved, and the SGS model is only required to capture universal small-scale features. However, between the surface and the lowest grid point within the flow, the turbulent motions are confined by the surface such that the SGS and wall models represent a majority of the dynamics. As a result, the velocities in the region very near the surface are subject to higher uncertainty than elsewhere in the domain. The validity of assumptions regarding inertial effects is also less certain close to the surface (Richter & Chamecki, 2018). To avoid the uncertainty of trajectories originating directly on the surface, we choose to restrict our analysis to the fate of particles after they reach the one meter starting height. The analysis is therefore focused on how gentle topography influences the intermediate processes connecting emitted particles to long-range transport as discussed in the introduction. Owing to the starting height, the particle statistics presented later do not account for the effects of topography and particle size on either the emission rate or particle dynamics within one meter of the surface. The study results are interpreted in the context of this design limitation.

Following the initiation of a particle trajectory, the position is evolved using Equations 1 and 2. The trajectory is terminated when the position intersects the bottom surface, that is, when the particle deposits. The trajectory is also terminated if the particle reaches the top of the domain. This upper boundary conditions affects a small number of particles within the sponge layer, which is not included in later results as discussed in Section 2.1.2. Due to the random placement, the initial x position is between 0 and $L_x = 2$ km. The particle follows the same horizontal periodic boundaries as the LES, and the trajectory is ended after traveling a total distance of 10 km in x, if not already terminated. A sample trajectory is shown in Figure 1.

In addition to the random horizontal starting position of particles, the starting time is uniformly distributed throughout the simulation time such that the particles undergo a representative sample of independent turbulent events. Owing to their gravitational settling, a majority of particles deposit on the surface after a small number of time steps. Thus, a large number of particles are required for converged statistics of long-lasting trajectories. To achieve the desired convergence, the number of released particles ranges from 1 million to 30 million across the nine combinations of topography and particle size. Where necessary, later results are presented as probabilities or fractions to account for the difference in number of released particles.

Smaller samples of particle trajectories were used to test the sensitivity of the later results to the choice of particle release height described above. Increasing the particle starting position from 1 to 5 m above the surface leads to small changes in the particle statistics. However, the changes are approximately equal across topography cases such that the quantitative differences between cases remain similar. Conclusions regarding topographical effects are therefore insensitive to the release height, noting again that these findings do not account for differences in emissions or dynamics within one meter of the surface.

3. Results

3.1. Vertical Flow Statistics

Average and root-mean-squared (r.m.s.) statistics for the vertical flow velocity are presented in Figure 2. For the flat case, the mean LES resolved velocity is $\tilde{W} = 0$ throughout the domain in Figure 2a. The r.m.s. $\sigma_{\tilde{w}}$, representing the intensity of turbulent fluctuations, is close to $\sigma_{\tilde{w}} \approx u_{*,o}$ in the bottom 150 m of the boundary layer in Figure 2b. This magnitude is consistent with typical values for the neutrally stratified surface layer (Kaimal & Finnigan, 1994).

The introduction of the hill creates a mean flow field generally conforming to the topography, with upward and downward flow on the uphill and downhill sides of the terrain, respectively. While the dipole behavior for $\tilde{W}$ is consistent with an inviscid potential flow, the asymmetry in both shape and intensity between the upward and downward flow regions is an effect of turbulence (Kaimal & Finnigan, 1994). Specifically, increased turbulent stresses in the hill wake cause the downflow region to have a smaller magnitude across a larger area than the upflow. The magnitude of $\tilde{W}$ relative to W_s is also noteworthy: The mean flow reaches magnitudes between $\tilde{W} \,/\, u_{*,o} \approx \pm(3-4)$ on either side of the small hill in Figure 2c and $\tilde{W} \,/\, u_{*,o} \approx \pm(6-8)$ on either side of the large hill in Figure 2e. Based on these values, the mean flow field around the hill is significantly stronger than the particle settling velocities $W_s \,/\, u_{*,o}$ listed in Table 2, even for the smaller hill and 60 μm particles. The $\tilde{W}$ fields suggest gentle topography is sufficient for the induced mean flow to influence particle transport, which is supported by later results.

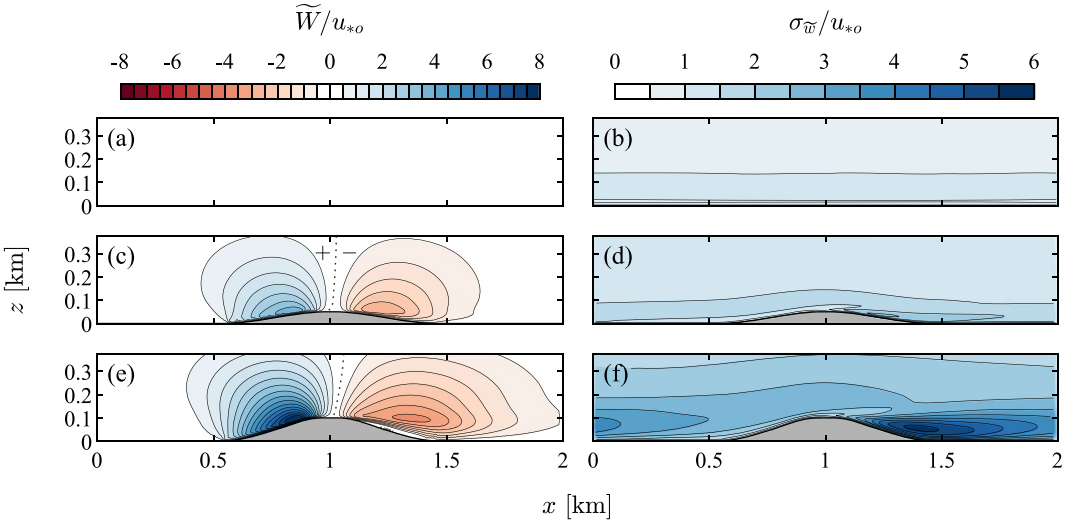

Figure 2. Large-eddy simulation resolved vertical velocity statistics normalized by the upstream shear velocity $u_{*,o}$. Columns correspond to the mean $\tilde{W}$ (a, c, e) and root-mean-squared (r.m.s.) $\sigma_{\tilde{w}}$ (b, d, f). Rows correspond to the flat (a and b), small hill (c and d), and large hill (e and f) topography cases.

The turbulent fluctuations also increase significantly in the presence of the hills. The increase in $\sigma_{\tilde{w}}$ from Figure 2b to Figures 2d and 2f is apparent throughout the domain, with the largest increase located in the highly turbulent wake downwind of the hill crest (Finnegan et al., 2020; Kaimal & Finnigan, 1994). The r.m.s. reaches values comparable to the magnitude of the mean $\tilde{W}$ in the wake: The r.m.s. is $\sigma_{\tilde{w}} \approx 2.5u_{*,o}$ for the small hill in Figure 2d and $\sigma_{\tilde{w}} \approx 5.5u_{*,o}$ for the large hill in Figure 2f. The wake region behind the large hill extends across the periodic boundary and reaches the upwind region near $x = 0.5$ km. The extended wake serves as a reminder that the flow statistics result from the compounding effect of encountering the hill numerous times in a periodic manner.

3.2. Particle Elevation

The primary question of the study is how topography affects the elevation of entrained coarse dust particles. This question is addressed here using statistics of the maximum height z'_{max} reached by each trajectory. Specifically, the probability density function (pdf) and cumulative distribution function (cdf) of z'_{max} were compiled using all the trajectories for each case. The probability a particle trajectory will reach above a given height z' is then defined as

$$\mathrm{P}(z'_{max} > z') = 1 - \mathrm{cdf}(z'_{max}) = \int_{z'}^{\infty} \mathrm{pdf}(z'_{max}) dz'_{\max}, \tag{4}$$

where the heights z' and z'_{max} are relative to the topography as shown in Figure 1. The upper limit of the integral is constrained by the domain depth in practice. The probability $\mathrm{P}(z'_{max} > z')$ is shown in Figure 3 for all nine case scenarios. The horizontal axes are scaled logarithmically to reveal a wide range of probabilities and emphasize the large differences between topography cases.

Topography increases the probability a 5 μm particle (dotted lines) will be transported above $z' = 200$ m by a factor between 1.8 (for the small hill) and 3.5 (large hill), compared to flat terrain. Similarly, the probability for a 20 μm particle (dashed lines) is increased by a factor between 2.3 and 5.3. Further, the observed differences in probability increase with increasing height above 200 m. The significant magnitude of these factors indicate that the effect of topography must be accounted for to accurately estimate atmospheric coarse dust concentrations.

The effect of topography on the coarsest particles is even greater: The probability a 60 μm particle (solid lines) will reach $z' = 200$ m is 0.0016% for the flat case, 0.15% for the small hill, and 2.4% for the large hill. These

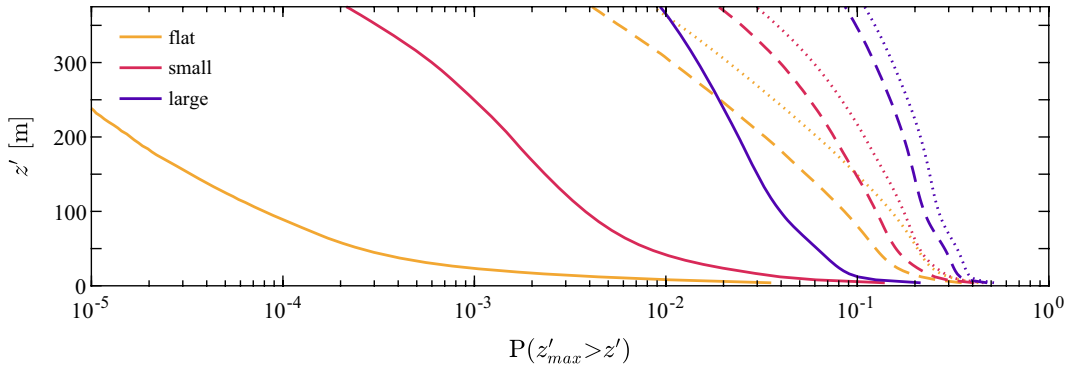

Figure 3. Probability $P(z'_{max} > z')$ that a particle trajectory reaches above a given height z', where the height is relative to the topography and z'_{max} is the maximum relative height along the trajectory. Line colors correspond to the topography cases, and line styles indicate the 5 μm (…), 20 μm (– – –), and 60 μm (—) particles.

numbers demonstrate that the presence of simple topography can increase the vertical transport of very coarse dust by orders of magnitude. Yet, a majority of the coarsest particles do not experience uplift, even in the presence of the large hill. The orders-of-magnitude difference in transport is therefore still confined to relatively rare turbulent events.

Figure 3 shows that the influence of topography becomes increasingly important with particle size. This trend across particles sizes is attributed to the $W_s \propto D_p^2$ functional dependence in the gravitation settling, where Table 2 shows the terminal settling speed is significantly increased for 60 μm particles and becomes similar in magnitude to the relevant velocity scale $u_{*,o}$. For the flat topography with $\tilde{W} = 0$ and $\sigma_{\tilde{w}} \approx u_{*,o}$, even under strong wind conditions the 60 μm particles have terminal settling speed $W_s \sim O(u_{*,o})$ and are too heavy to be lifted by near-surface turbulence. It is for these coarser particles that an enhancement of transport due to topography becomes especially relevant.

As a reminder, the particles in this study are randomly released above the surface such that the probabilities in Figure 3 do not reflect either the emission process or dynamics very near the surface below the 1 m release height. The probability values pertain only to the fate of released particles and do not include any contribution from enhanced surface stresses. Accounting for increased surface stresses may further enhance the effect of topography on the probabilities in Figure 3, as discussed later.

3.3. Mechanisms for Vertical Transport

The particle height statistics in Figure 3 demonstrate the strong impact of topography on the likelihood a coarse dust particle is elevated, but the question remains as to *how* these particles are transported. The remainder of the analysis explores the topographical flow mechanisms responsible for increasing vertical transport. To illustrate these mechanisms, only high-reaching particle trajectories are considered here, based on particles that exceed $z' = 200$ m at any point along their trajectory. The spatial distribution of these particle trajectories is represented by a joint pdf (jpdf) in x and z, compiled from all the particle positions along the trajectories. The resulting joint distributions are shown in Figure 4 for 60 μm particles in each topography case. Only two periodic domain lengths are shown in the figure to more easily visualize the topography trends. The specific trend of interest is how the regions of high joint probability change along the shape of the topography in x to reveal a transport "pathway."

As expected, the pathway for the flat case in Figure 4a approximately follows an inclined trajectory with shallow slope. The breadth of the high-probability region is partially explained by the variation in initial particle position between $x = 0$–2 km. The near-zero probability at $x = 0$ and the probability peak around $x = 2$ km reflect the accumulation of previously released particles due to downwind transport. Note that the particles reach the $z' = 200$ m threshold beyond the $x = 4$ km range shown in the figure.

In comparison with the flat case, three potential mechanisms for enhancing particle uplift are observed in Figures 4b and 4c: (I) uplift by the mean wind conforming to the hill slope; (II) ejection downwind of the

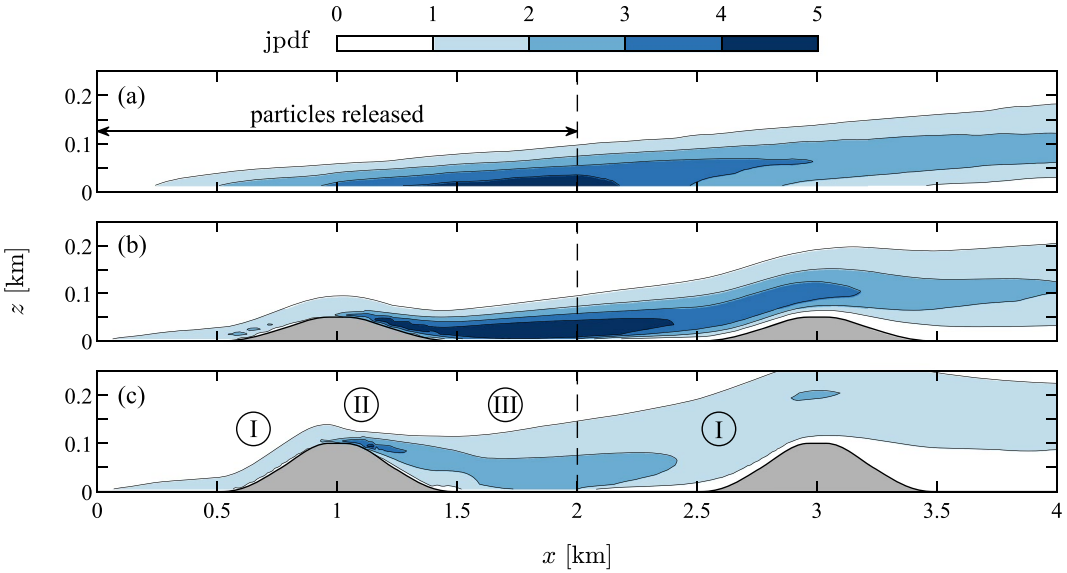

Figure 4. Distribution of particle positions along high-reaching trajectories for the 60 μm particles: (a) flat case featuring 0.0016% of total trajectories; (b) small hill case (0.15% of trajectories); (c) large hill case (2.4% of trajectories). A trajectory is considered high-reaching if it exceeds $z' = 200$ m at any point. The plotted field show trajectories spanning two lengths of the periodic large-eddy simulation domain. The field is limited to the bottom half of the domain and the aspect ratio is stretched by a factor of two to enhance visualization.

hill crest; and (III) enhanced dispersion by turbulence in the wake of the hill. These effects are compounding, where for instance the dispersion of particles in the wake of the first hill leads to higher uplift along the subsequent hill at $x = 2.5$–3 km. Each of these three mechanisms are further evaluated in the following subsections.

3.3.1. Mechanism I: Uplift by the Mean Wind

The influence of the mean flow field was already suggested in Section 3.1 and Figure 2, where the positive flow region on the uphill side of the topography exceeds the terminal settling speed of coarse dust particles. Figures 4b and 4c substantiate the previous findings, demonstrating the high-reaching particle trajectories generally follow the same trends as $\tilde{W}$. Importantly, this mean flow mechanism only acts on emitted particles away from the surface. The mean $\tilde{W}$ is close to zero at the surface and thus does not directly contribute to particle emission.

To further investigate the impact of the mean flow, Figure 5 shows probability distributions of the first longitudinal position x_1 where the high-reaching trajectories exceed $z = 200$ m. For this statistic, the height threshold is absolute with respect to the flat surface rather than relative to the topography (i.e., z'). This choice is due to the fact that the mean flow field and particle uplift result from the topography shape, such that selecting the relative elevation would subtract from the shape and mean flow effect and lead to potentially misleading results.

Two trends are apparent in Figure 5: The topography provides a preferential location for particle uplift corresponding to the mean flow field and a shorter pathway to higher elevations. The strong peaks in the distributions for the hill cases are consistently aligned with the uphill region of the topography where $\tilde{W}$ is most positive. The pdf shape is the same between particle sizes, where the only difference is the fraction of particles that reach $z = 200$ m and are represented in the figure.

The second trend is the skewness of the distributions toward smaller x_1 values for the hill cases in Figure 5. In addition to significantly increasing the likelihood coarse dust will be transported above $z = 200$ m (Figure 3), the hills shorten the distance x_1 required for the particle to reach this elevation. Further, the distance decreases with increasing hill height H. In other words, hill topography leads to faster (in x) vertical

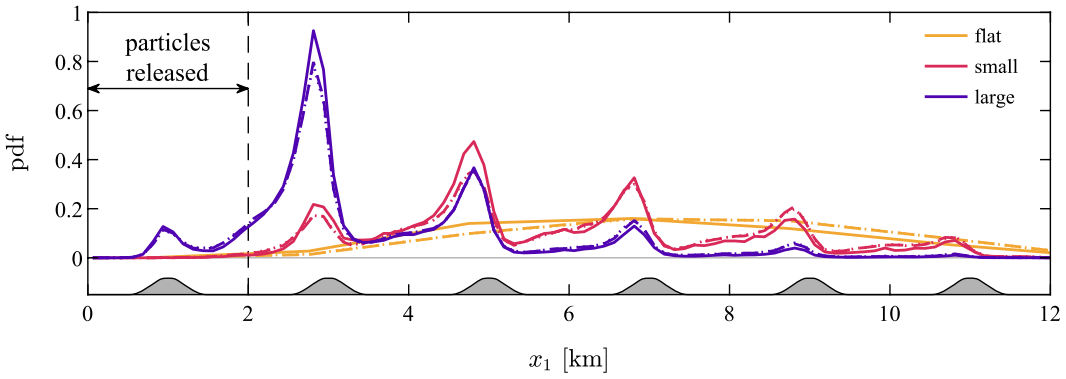

Figure 5. Distribution of the first streamwise position x_1 where the tracked particles exceed $z = 200$ m. Line colors correspond to the topography cases, and line styles indicate the 5 μm (…), 20 μm (– – –), and 60 μm (—) particles. The distributions for the 5 and 20 μm particles are nearly identical and appear as a dash-dotted line.

spreading of the particle trajectories, thus increasing the effective vertical dispersion at the scale of the domain. The more localized dispersion specific to the hill wake is assessed later.

3.3.2. Mechanism II: Ejection From the Hill Crest

The remaining mechanisms relate to the flow wake region downwind of the hill crest. To isolate the dynamics in this region, the trajectories considered here are limited to particles released within 25 m of the hill crest. This initial particle position corresponds to the top of the hill or the equivalent location in the flat case. Unlike the previous results, all trajectories are included in the following analysis and are not filtered by their elevation. Based on the same procedure for computing the jpdf as in Figure 4, the jpdfs for particles released at the crest are shown in Figures 6a and 6b.

For the smaller hill in Figure 6a, the most probable trajectory is approximately aligned with the hillslope. In contrast, the most probable trajectory for the larger hill in Figure 6b initially moves outward away from the hill and thereafter decreasing more slowly in height than the hillslope. The same qualitative behavior is also visible in Figures 4b and 4c trajectories. The difference between hill cases is due to the flow separation reflected by the reversed flow $\tilde{U} < 0$ in Figure 1. The separation is also apparent from the mean flow in Figure 2e, where the positive $\tilde{W}$ contours are visibly displaced from the hillslope. The mean flow leading to the dipole behavior in $\tilde{W}$ effectively senses the separation region as part of the hill such that the mean downflow does not impinge on the separation region (Kaimal & Finnigan, 1994). Rather than remaining attached to the hill surface, the mean flow conforms to the shape of the separation region. The flow separation thus allows the average particle at the hill crest to "eject" away from the hill and along the boundary of the separation region as observed in Figures 6b and 4c. Compared to the attached flow case observed in Figure 6a, the particle is ejected into a higher position in the hill wake, increasing the likelihood of further vertical transport. Scalar transport is maximized at the point of flow separation (Ross, 2011), and a similar effect is expected for heavier particles such as coarse dust. For the present hill length L and roughness z_o, the larger hill with maximum slope $\theta_{max} = 19°$ is nominally steeper than the critical condition for flow separation. This critical slope increases (or decreases) with increasing (decreasing) L / z_o (Wood, 1995).

Another consideration for the crest ejection is the local surface stress. The impact of the hill crest on particle transport is apparent in Figures 4b and 4c, even with the dust particles released at random locations independent of the surface stress. The maximum stress occurs just upwind of the crest, and the stress along the crest reaches several times larger than the upstream condition given by $u_{*,o}$ (see, e.g., Gloerfelt & Cinnella, 2019; Taylor, 1977). Therefore, in addition to being a favorable pathway for transport, the stress along the crest may increase entrainment. If the present simulations modeled emission from the surface, the enhanced stress would emit more particles along the crest than in the flat case, thus leading to a greater number of particles subsequently ejected into the wake and an even larger effect of topography on vertical transport than suggested by Figure 3. This increased entrainment assumes that the erodible material is uniformly distributed across the topography (e.g., desert dunes). The effect on entrainment may be diminished in cases when the erodible particles are predominately concentrated within the topographic depressions.

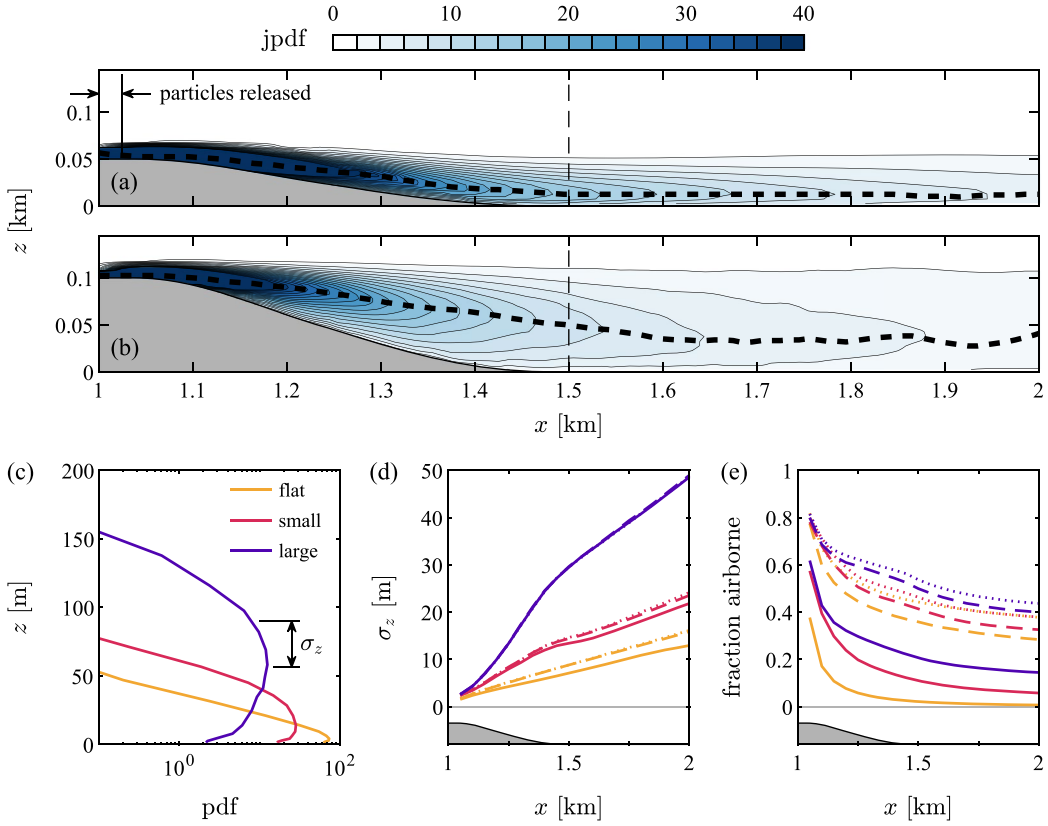

Figure 6. Dispersion of particles released from the hill crest. (a and b) Distribution of particle trajectory positions for the 60 μm particles in the (a) Large hill and (b) Small hill cases, where the thick dotted lines indicate the most probable trajectory. (c) Distribution of vertical position for 60 μm particles at $x = 1.5$ km which is indicated by a dashed vertical line in (a and b). (d) Standard deviation of particle position σ_z as a function of distance from the crest. (e) Probability a particle ejected from the crest is airborne, that is, not deposited, as a function of the distance from the crest. Line colors correspond to the topography cases, and line styles indicate the 5 μm (…), 20 μm (– – –), and 60 μm (—) particles.

3.3.3. Mechanism III: Enhanced Dispersion by Wake Turbulence

Once a particle enters the hill wake, its trajectory undergoes strong turbulent fluctuations as quantified by $\sigma_{\tilde{w}}$ in Figure 2. In considering the ensemble of particles released at the crest, these fluctuations increase the spread of the particle position. For example, Figure 6c shows the distribution of particle height for the position $x = 1.5$ km in Figures 6a and 6b. As a reminder, only particles released at the hilltop are considered here. The large hill case exhibits a significantly wider spread in particle height than the other cases, indicating increased dispersion. The dispersion is quantified here by σ_z, the standard deviation of the height distribution in Figure 6c (Pan et al., 2014). To account for the fact that the distribution shape is incomplete due to the imposed boundary at $z' = 0$, the dispersion can instead be estimated using a Gaussian distribution fitting algorithm on the position pdfs. The same qualitative trend in σ_z is observed for both methods. However, the results of the Gaussian fit are more uncertain far from the crest where the pdfs are not fully converged, and thus the simpler σ_z definition is presented.

Figure 6d shows σ_z as a function of position x downwind of the hill crest. The increasing turbulence trend in $\sigma_{\tilde{w}}$ across the topography cases is reflected by the dispersion σ_z. The enhanced dispersion increases vertical transport and the number of particles reaching higher elevations. Due to the approximate symmetry of the particle plume ejected from the crest, the downward transport of particles below the plume centerline is also increased, which accelerates their deposition. However, the upward transport component is of greater interest for the present work.

The dispersion in Figure 6d exhibits only a weak dependence on particle size. This suggests the relaxation time t_p of the particles is sufficiently small such that the particles respond in the same way, regardless of their size, to the fluctuating wake velocities primarily responsible for dispersion. The weak size dependence is also due to the methodology for estimating σ_z, where a deposited particle is excluded from the σ_z calculations downstream of where it deposited. The size dependence is more apparent in Figure 6e showing the number of particles remaining airborne. More than 30% of 5 and 20 μm particles remain airborne after 1 km travel distance, while a greater majority of 60 μm particles are deposited before then.

An animation is included with the manuscript as supplemental material to facilitate visualization of the ejection and dispersion processes in the hill wake. The animation shows 20,000 trajectories for 60 μm particles released at the hill crest. The trajectories span a range of y positions and starting times such that the animation represents the effect of an ensemble of turbulence events.

4. Conclusions and Implications for Atmospheric Dust Models

Under neutrally stratified conditions and flat topography, there is an absence of persistently strong vertical flow patterns, even under high wind conditions (i.e., $U(z = 10\text{ m}) \approx 8$ m/s in this study). Accordingly, only a small number of coarse dust particles are transported from near the surface ($z = 1$ m) to higher elevations ($z \sim O(100\text{ m})$). Hill topography induces the strong vertical motions necessary for transport via multiple mechanisms. Even for gentle topography, the mean upward flow along the hillslope is sufficient to lift coarse dust above the hill, and the highly turbulent wake region enhances dispersion and increases the upward trajectory of many particles. For steeper hills with a recirculation region downwind of the crest, the flow separation creates the additional effect of ejecting particles away from the hill and higher into the wake relative to the surface. These mechanisms are not exclusive to the coarse mineral dust which motivated the study, and are equally applicable to other heavy aerosols and particles such as pollen.

With respect to increased transport, the topography mechanisms are significantly more efficient than increased wind speed. The wind in flat terrain would need to be 3–6 times stronger to match the turbulent intensity of the hill wake in the topography cases tested here, and even then the flat terrain would lack the uplift of the mean windward flow. Owing to these advantages, gentle hill topography can increase the number of 5 and 20 μm coarse dust particles reaching high altitudes by 200%–500%. For even coarser 60 μm particles approaching the regime of giant dust, the difference in transport due to topography grows to be orders of magnitude. We note that these quantitative differences are specific to the two-dimensional, periodic topographies studied here. Further investigation is required to assess how much the enhancement of transport would be modified by variations such as longer distances between hills, three-dimensional topography, or a single isolated hill.

While topography alone can significantly increase transport, the fraction of particles reaching several hundred meters above the surface is still relatively small, for example, ∼2% for the 60 μm particles. In this sense, hill topography is not expected to entirely explain the transport of coarse dust into the free atmosphere, where long-range transoceanic transport occurs (Engelstaedter et al., 2006; Perry et al., 1997). Rather, we expect topography to play a key dynamical role in the near-surface region, where the transport mechanisms discussed here connect entrained dust above the surface with large-scale thermal motions higher in the convective boundary layer, which thereafter lift dust to the free atmosphere (Freire et al., 2016; Klose & Shao, 2013; Lindau et al., 2021).

The importance of this intermediate transport mechanism is supported by recent observations of 100 μm dust at high altitudes (Rosenberg et al., 2014; Ryder et al., 2018; van der Does et al., 2018). Rosenberg et al. (2014) specifically suggested topography may enhance transport, and the present study unambiguously confirms that topography provides an efficient pathway for lifting coarse, heavy particles. These findings demonstrate the necessity for atmospheric dust models to include effects of topography. Parameterizing these effects is not trivial, however. In the idealized two-dimensional topography employed here, the effective vertical dispersion results from complex dependencies on the hill shape, hill size, and distance between hills. The effect of topography would be further complicated by incorporating vegetation, three-dimensional topography, and misalignment between the wind and the topography which induces secondary flows (Rotach et al., 2008). Additionally, this work does not consider heterogeneity of the surface topography which would

exist within the subgrid-scales of atmospheric models. It is currently unclear whether the impact of topography heterogeneity on particle transport can be accurately represented by existing methodologies such as mosaic and tile approaches (Avissar & Pielke, 1989).

Considering the topography effects observed in this study are not represented in current models, a relatively simple parameterization that neglects these complications listed above may be sufficient to correct for a majority of the coarse dust underestimation. To this end, the increased transport can be condensed into an enhanced dispersion due to turbulence and the mechanisms presented here. It may be possible to characterize the enhanced dispersion of entrained particles in terms of a factor increase above the case of flat terrain. This dispersion factor may be coarsely approximated as a function of the statistical properties for the complex subgrid-scale topography, for example, the standard deviation of the surface elevation, and the factor would additionally depend on the particle size. The investigation of these dependencies across a wider range of topography and particle size is the subject of future work.

Appendix A: Large-Eddy Simulation Test Case

As discussed in Section 2.1.2, the hill shape selected for this study is common in computational flow literature. Owing to the computational challenge posed by the hill's steep slope (for which flow separation occurs) and the availability of high-resolution experiments to validate results, the shape has been used as a benchmark case for several modeling projects and workshops. These previous literature are used to validate the immersed boundary treatment of the present LES code.

The specific reference results presented here for comparison are those of Gloerfelt and Cinnella (2019). The authors validated their results against multiple previous studies, including a direct numerical simulation of the flow (Krank et al., 2018). The simulation by Gloerfelt and Cinnella (2019) comprised wall-resolved LES with a curvilinear coordinate system conforming to the topography on a high-resolution $512 \times 256 \times 256$ numerical grid. Considering the test conditions for the present code include wall-modeled LES with an immersed boundary on a relatively lower resolution $256 \times 128 \times 128$ grid, the comparison constitutes a rigorous assessment of the code.

A comparison of LES resolved mean and r.m.s. velocities is shown in Figure A1. Each statistic is normalized by the depth-averaged mean velocity above the hill at $x = 0$. An important difference in the comparison is the treatment of the upper boundary condition. Gloerfelt and Cinnella (2019) employed an upper wall boundary to create a closed channel to be consistent with previous experiments (Rapp & Manhart, 2011). The same closed channel setup is not feasible in the present in-house code, and the upper boundary was instead approximated using a sponge layer. While this approximation leads to close matching of the streamwise mean $\tilde{U}$ in Figure A1a, the sponge layer may be responsible for the small differences in $\tilde{W}$ and $\sigma_{\tilde{u}}$ above $z = H$.

Differences in vertical velocities $\tilde{W}$ and $\sigma_{\tilde{w}}$ in the wake of the hill may be due to resolution. Besides these differences, however, the present LES captures well the trends relevant to this study: the recirculation region with $\tilde{U} < 0$ extending to $x = 4H$, the positive upward flow at $x = 8H$, downward flow at $x = 3H - 6H$, and enhanced turbulence emanating outward from the hill crest. These trends are matched quantitatively with the reference results, thus demonstrating the reliability of the LES results for the present study.

To achieve a realistic gentle topography within the atmospheric boundary layer, the hill in the main study occupies a smaller portion of the domain than in the test case. This rescaling leads the main simulations to have a coarser resolution with respect to the hill dimensions than the test case. However, it is also worth recalling that the LES setup for the hill cases in Table 1 are computationally less challenging than the test case in Figure A1. The large hill topography is 60% less steep than the test case, resulting in a smaller flow separation region and a weaker turbulence peak at the hill crest. The weaker turbulence specifically alleviates the resolution required to resolve the majority of the fluctuating energy in the wake. The hill cases in Table 1 were executed for various grid resolutions and aspect ratio to test the convergence of the simulations, for example, between a $256 \times 128 \times 128$ and a $320 \times 160 \times 160$ grid. The tests confirmed the present

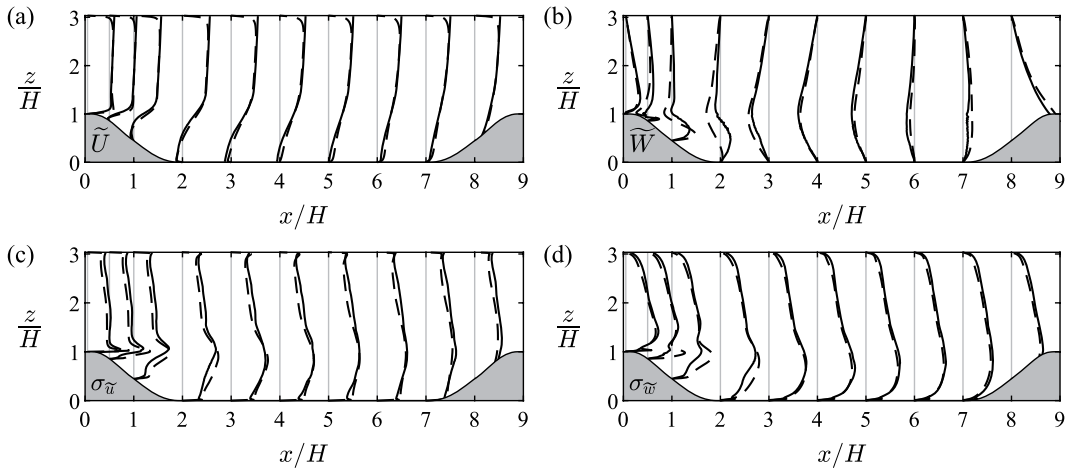

Figure A1. Large-eddy simulation resolved velocity profiles for the periodic hill test case at the 10 streamwise x positions indicated by vertical lines: (a) Streamwise mean $\tilde{U}$; (b) Vertical mean $\tilde{W}$; (c) Streamwise root-mean-squared (r.m.s.) $\sigma_{\tilde{u}}$; (d) vertical r.m.s. $\sigma_{\tilde{w}}$. The present code results (solid lines) are compared against Gloerfelt and Cinnella (2019, dashed lines).

simulations capture the main features of the flow relevant to the study, with no qualitative changes across the tested resolutions.

Data Availability Statement

The data required to reproduce the figures are available from the Dryad repository at the assigned https://doi.org/10.5068/D15Q4C. Additional data inquiries should be directed to the corresponding author.

Acknowledgments
The authors gratefully acknowledge funding from the Cold Regions Research and Engineering Laboratory (contract W913E520C0001) and the U.S. Army Research Laboratory (grant W911NF2020150). The views and conclusions contained in this document are those of the authors and should not be interpreted as representing the official policies, either expressed or implied, of the Army Research Laboratory or the U.S. Government.

References

Adebiyi, A. A., & Kok, J. F. (2020). Climate models miss most of the coarse dust in the atmosphere. *Science Advance*, *6*(15), eaaz9507. https://doi.org/10.1126/sciadv.aaz9507

Albertson, J. D., & Parlange, M. B. (1999). Surface length scales and shear stress: Implications for land-atmosphere interaction over complex terrain. *Water Resources Research*, *35*(7), 2121–2132. https://doi.org/10.1029/1999WR900094

Ansmann, A., Rittmeister, F., Engelmann, R., Basart, S., Jorba, O., Spyrou, C., et al. (2017). Profiling of Saharan dust from the Caribbean to western Africa—Part 2: Shipborne Lidar measurements versus forecasts. *Atmospheric Chemistry and Physics*, *17*(24), 14987–15006. https://doi.org/10.5194/acp-17-14987-2017

Avissar, R., & Pielke, R. A. (1989). A parameterization of heterogeneous land surfaces for atmospheric numerical models and its impact on regional meteorology. *Monthly Weather Review*, *117*(10), 2113–2136. https://doi.org/10.1175/1520-0493(1989)117⟨2113:APOHLS⟩2.0.CO;2

Bailey, B. N. (2017). Numerical considerations for Lagrangian stochastic dispersion models: Eliminating rogue trajectories, and the importance of numerical accuracy. *Boundary-Layer Meteorology*, *162*, 43–70. https://doi.org/10.1007/s10546-016-0181-6

Beljaars, A. C. M., Brown, A. R., & Wood, N. (2004). A new parametrization of turbulent orographic form drag. *The Quarterly Journal of the Royal Meteorological Society*, *130*(599), 1327–1347. https://doi.org/10.1256/qj.03.73

Betzer, P. R., Carder, K. L., Duce, R. A., Merrill, J. T., Tindale, M., Uematsu, N. W., et al. (1988). Long-range transport of giant mineral aerosol particles. *Nature*, *336*, 568–571. https://doi.org/10.1038/336568a0

Bou-Zeid, E., Meneveau, C., & Parlange, M. (2005). A scale-dependent Lagrangian dynamic model for large eddy simulation of complex turbulent flows. *Physics of Fluids*, *17*(2), 025105. https://doi.org/10.1063/1.1839152

Breuer, M., Peller, N., Rapp, C., & Manhart, M. (2009). Flow over periodic hills—Numerical and experimental study in a wide range of Reynolds numbers. *Computers & Fluids*, *38*(2), 433–457. https://doi.org/10.1016/j.compfluid.2008.05.002

Chen, B., Chamecki, M., & Katul, G. G. (2019). Effects of topography on in-canopy transport of gases emitted within dense forests. *The Quarterly Journal of the Royal Meteorological Society*, *145*(722), 2101–2114. https://doi.org/10.1002/qj.3546

Chen, B., Chamecki, M., & Katul, G. G. (2020). Effects of gentle topography on forest-atmosphere gas exchanges and implications for eddy-covariance measurements. *Journal of Geophysical Research: Atmospheres*, *125*(11), e2020JD032581. https://doi.org/10.1029/2020JD032581

Chester, S., Meneveau, C., & Parlange, M. B. (2007). Modeling turbulent flow over fractal trees with renormalized numerical simulation. *Journal of Computational Physics*, *225*, 427–448. https://doi.org/10.1016/j.jcp.2006.12.009

Clift, R., Grace, J., & Weber, M. E. (2005). *Bubbles, drops, and particles*. Dover Publications, Inc.

Comola, F., Giometto, M. G., Salesky, S. T., Parlange, M. B., & Lehning, M. (2019). Preferential deposition of snow and dust over hills: Governing processes and relevant scales. *Journal of Geophysical Research: Atmospheres*, *124*(14), 7951–7974. https://doi.org/10.1029/2018JD029614

Deardorff, J. W. (1970). A numerical study of three-dimensional turbulent channel flow at large Reynolds numbers. *Journal of Fluid Mechanics*, *41*(2), 453–480. https://doi.org/10.1017/S0022112070000691

Denjean, C., Cassola, F., Mazzino, A., Triquet, S., Chevaillier, S., Grand, N., et al. (2016). Size distribution and optical properties of mineral dust aerosols transported in the western Mediterranean. *Atmospheric Chemistry and Physics*, *16*(2), 1081–1104. https://doi.org/10.5194/acp-16-1081-2016

Engelstaedter, S., Tegen, I., & Washington, R. (2006). North African dust emissions and transport. *Earth-Science Reviews*, *79*(1), 73–100. https://doi.org/10.1016/j.earscirev.2006.06.004

Finnegan, J., Ayotte, K., Harman, I., Katul, G. G., Oldroyd, H., Patton, E., et al. (2020). Boundary-layer flow over complex topography. *Boundary-Layer Meteorology*, *177*, 247–313. https://doi.org/10.1007/s10546-020-00564-3

Freire, L. S., Chamecki, M., & Gillies, J. A. (2016). Flux-profile relationship for dust concentration in the stratified atmospheric surface layer. *Boundary-Layer Meteorology*, *160*, 249–267. https://doi.org/10.1007/s10546-016-0140-2

Frölich, J., Mellen, C. P., Rodi, W., Temmerman, L., & Leschziner, M. A. (2005). Highly resolved large-eddy simulation of separated flow in a channel with streamwise periodic constrictions. *Journal of Fluid Mechanics*, *526*, 19–66. https://doi.org/10.1017/S0022112004002812

Ginoux, P., Chin, M., Tegen, I., Prospero, J. M., Holben, B., Dubovik, O., & Lin, S.-J. (2001). Sources and distributions of dust aerosols simulated with the GOCART model. *Journal of Geophysical Research*, *106*(D17), 20255–20273. https://doi.org/10.1029/2000JD000053

Gloerfelt, X., & Cinnella, P. (2019). Large eddy simulation requirements for the flow over periodic hills. *Flow, Turbulence and Combustion*, *109*, 55–91. https://doi.org/10.1007/s10494-018-0005-5

Hölzer, A., & Sommerfeld, M. (2008). New simple correlation formula for the drag coefficient of non-spherical particles. *Powder Technology*, *184*(3), 361–365. https://doi.org/10.1016/j.powtec.2007.08.021

Huang, Y., Adebiyi, A. A., Formenti, P., & Kok, J. F. (2021). Linking the different diameter types of aspherical desert dust indicates that models underestimate coarse dust emission. *Geophysical Research Letters*, *48*(6), e2020GL092054. https://doi.org/10.1029/2020GL092054

Huang, Y., Kok, J. F., Kandler, K., Lindqvist, H., Nousiainen, T., Sakai, T., et al. (2020). Climate models and remote sensing retrievals neglect substantial desert dust asphericity. *Geophysical Research Letters*, *47*(6), e2019GL086592. https://doi.org/10.1029/2019GL086592

Huneeus, N., Schulz, M., Balkanski, Y., Griesfeller, J., Prospero, J., Kinne, S., et al. (2011). Global dust model intercomparison in AeroCom phase I. *Atmospheric Chemistry and Physics*, *11*(15), 7781–7816. https://doi.org/10.5194/acp-11-7781-2011

Hunt, J. C. R., & Snyder, W. H. (1980). Experiments on stably and neutrally stratified flow over a model three-dimensional flow. *Journal of Fluid Mechanics*, *96*(4), 671–704. https://doi.org/10.1017/S0022112080002303

Jickells, T., Boyd, P., & Hunter, K. A. (2014). Biogeochemical impacts of dust on the global carbon cycle. In P. Knippertz, & J.-B. W. Stuut (Eds.), *Mineral dust* (pp. 359–384). Springer. https://doi.org/10.1007/978-94-017-8978-3_14

Jiménez, P. A., & Dudhia, J. (2012). Improving the representation of resolved and unresolved topographic effects on surface wind in the WRF model. *Journal of Applied Meteorology and Climatology*, *51*(2), 300–316. https://doi.org/10.1175/JAMC-D-11-084.1

Jung, E., Albrecht, B., Prospero, J. M., Jonsson, H. H., & Kreidenweis, S. M. (2013). Vertical structure of aerosols, temperature, and moisture associated with an intense African dust event observed over the eastern Caribbean. *Journal of Geophysical Research: Atmospheres*, *118*(10), 4623–4643. https://doi.org/10.1002/jgrd.50352

Kähler, C. J., Scharnowski, S., & Cierpka, C. (2016). Highly resolved experimental results of the separated flow in a channel with streamwise periodic constrictions. *Journal of Fluid Mechanics*, *796*, 257–284. https://doi.org/10.1017/jfm.2016.250

Kaimal, J. C., & Finnigan, J. J. (1994). *Atmospheric boundary layer flows*. Oxford University Press.

Kandler, K., Benker, N., Bundke, U., Cuevas, E., Ebert, M., Knippertz, P., et al. (2007). Chemical composition and complex refractive index of Saharan mineral dust at Izaña, Tenerife (Spain) derived by electron microscopy. *Atmospheric Environment*, *41*(37), 8058–8074. https://doi.org/10.1016/j.atmosenv.2007.06.047

Katul, G. G., Finnigan, J. J., Poggi, D., Leuning, R., & Belcher, S. E. (2006). The influence of hilly terrain on canopy-atmosphere carbon dioxide exchange. *Boundary-Layer Meteorology*, *118*, 189–216. https://doi.org/10.1007/s10546-005-6436-2

Klose, M., & Shao, Y. (2013). Large-eddy simulation of turbulent dust emission. *Aeolian Research*, *8*, 49–58. https://doi.org/10.1016/j.aeolia.2012.10.010

Kok, J. F. (2011). A scaling theory for the size distribution of emitted dust aerosols suggest climate models underestimate the size of the global dust cycle. *Proceedings of the National Academy of Sciences of the United States of America*, *108*(3), 1016–1021. https://doi.org/10.1073/pnas.1014798108

Kok, J. F., Adebiyi, A. A., Albani, S., Balkanski, Y., Checa-Garcia, R., Chin, M., et al. (2021). Improved representation of the global dust cycle using observational constraints on dust properties and abundance. *Atmospheric Chemistry and Physics*, *21*, 8127–8167. https://doi.org/10.5194/acp-21-8127-2021

Kok, J. F., Parteli, E. J. R., Michaels, T. I., & Bou Karam, D. (2012). The physics of wind-blown sand and dust. *Reports on Progress in Physics*, *75*, 106901. https://doi.org/10.1088/0034-4885/75/10/106901

Kok, J. F., Ridley, D. A., Zhou, Q., Miller, R. L., Zhao, C., Heald, C. L., et al. (2017). Smaller desert dust cooling effect estimated from analysis of dust size and abundance. *Nature Geoscience*, *10*(4), 274–278. https://doi.org/10.1038/ngeo2912

Krank, B., Kronbichler, M., & Wall, W. A. (2018). Direct numerical simulation of flow over periodic hills up to $Re_H = 10{,}595$. *Flow, Turbulence and Combustion*, *101*, 521–551. https://doi.org/10.1007/s10494-018-9941-3

Li, Q., Bou-Zeid, E., & Anderson, W. (2016). The impact and treatment of the Gibbs phenomenon in immersed boundary method simulations of momentum and scalar transport. *Journal of Computational Physics*, *310*, 237–251. https://doi.org/10.1016/j.jcp.2016.01.013

Lilly, D. K. (1966). *The representation of small-scale turbulence in numerical simulation experiments (Manuscript No. 281)*. National Center for Atmospheric Research. https://doi.org/10.5065/D62R3PMM

Lindau, F. G. L., Simões, J. C., Delmonte, B., Ginot, P., Baccolo, G., Paleari, C. I., et al. (2021). Giant dust particles at Nevado Illimani: A proxy of summertime deep convection over the Bolivian Altiplano. *The Cryosphere*, *15*(3), 1383–1397. https://doi.org/10.5194/tc-15-1383-2021

Mahowald, N. M., Albani, S., Kok, J. F., Engelstaeder, S., Scanza, R., Ward, D. S., & Flanner, M. G. (2014). The size distribution of desert dust aerosols and its impact on the Earth system. *Aeolian Research*, *15*, 53–71. https://doi.org/10.1016/j.aeolia.2013.09.002

Mahowald, N. M., & Kiehl, L. M. (2003). Mineral aerosol and cloud interactions. *Geophysical Research Letters*, *30*(9). https://doi.org/10.1029/2002GL016762

Maring, H., Savoie, D. L., Izaguirre, M. A., Custals, L., & Reid, J. S. (2003). Mineral dust aerosol size distribution change during atmospheric transport. *Journal of Geophysical Research*, *108*(D19), 8592. https://doi.org/10.1029/2002JD002536

Mason, P. J., & Callen, N. S. (1986). On the magnitude of the subgrid-scale eddy coefficient in large-eddy simulations of turbulent channel flow. *Journal of Fluid Mechanics*, *162*, 439–462. https://doi.org/10.1017/S0022112086002112

Mittal, R., & Iaccarino, G. (2005). Immersed boundary methods. *Annual Review of Fluid Mechanics*, *37*, 239–261. https://doi.org/10.1146/annurev.fluid.37.061903.175743

Pan, Y., Chamecki, M., & Isard, S. A. (2014). Large-eddy simulation of turbulence and particle dispersion inside the canopy roughness layer. *Journal of Fluid Mechanics*, *753*, 499–534. https://doi.org/10.1017/jfm.2014.379

Perry, K. D., Cahill, T. A., Eldred, R. A., Dutcher, D. D., & Gill, T. E. (1997). Long-range transport of North African dust to the eastern United States. *Journal of Geophysical Research*, *102*(D10), 11225–11238. https://doi.org/10.1029/97JD00260

Rapp, C., & Manhart, M. (2011). Flow over periodic hills: An experimental study. *Experiments in Fluids*, *51*, 247–269. https://doi.org/10.1007/s00348-011-1045-y

Richter, D., & Chamecki, M. (2018). Inertial effects on the vertical transport of suspended particles in a turbulent boundary layer. *Boundary-Layer Meteorology*, *167*, 235–256. https://doi.org/10.1007/s10546-017-0325-3

Rosenberg, P. D., Parker, D. J., Ryder, C. L., Marsham, J. H., Garcia-Carreras, L., Dorsey, J. R., et al. (2014). Quantifying particle size and turbulent scale dependence of dust flux in the Sahara using aircraft measurements. *Journal of Geophysical Research: Atmospheres*, *119*(12), 7577–7598. https://doi.org/10.1002/2013JD021255

Ross, A. N. (2011). Scalar transport over forested hills. *Boundary-Layer Meteorology*, *141*, 179–199. https://doi.org/10.1007/s10546-011-9628-y

Rotach, M. W., Andretta, M., Calanca, P., Weigel, A. P., & Weiss, A. (2008). Boundary layer characteristics and turbulent exchange mechanisms in highly complex terrain. *Acta Geophysica*, *56*(1), 194–219. https://doi.org/10.2478/s11600-007-0043-1

Ryder, C. L., Highwood, E. J., Walser, A., Seibert, P., Philipp, A., & Weinzierl, B. (2019). Coarse and giant particles are ubiquitous in Saharan dust export regions and are radiatively significant over the Sahara. *Atmospheric Chemistry and Physics*, *19*(24), 15353–15376. https://doi.org/10.5194/acp-19-15353-2019

Ryder, C. L., Marenco, F., Brooke, J. K., Estelles, V., Cotton, R., Formenti, P., et al. (2018). Coarse-mode mineral dust size distributions, composition and optical properties from AER-D aircraft measurements over the tropical eastern Atlantic. *Atmospheric Chemistry and Physics*, *18*(23), 17225–17257. https://doi.org/10.5194/acp-18-17225-2018

Sawford, B. L., & Guest, F. M. (1991). Lagrangian statistical simulation of the turbulent motion of heavy particles. *Boundary-Layer Meteorology*, *54*, 147–166. https://doi.org/10.1007/BF00119417

Smagorinsky, J. (1963). General circulation experiments with the primitive equations: I. The basic experiment. *Monthly Weather Review*, *91*(3), 99–164. https://doi.org/10.1175/1520-0493(1963)091⟨0099:GCEWTP⟩2.3.CO;2

Sodemann, H., Lai, T. M., Marenco, F., Ryder, C. L., Flamant, C., Knippertz, P., et al. (2015). Lagrangian dust model simulations for a case of moist convective dust emission and transport in the western Sahara region during Fennec/LADUNEX. *Journal of Geophysical Research: Atmospheres*, *120*(12), 6117–6144. https://doi.org/10.1002/2015JD023283

Stull, R. B. (1988). *An introduction to boundary layer meteorology*. Kluwer Academic Publishers. https://doi.org/10.1007/978-94-009-3027-8

Swap, R., Garstang, M., Greco, S., Talbot, R., & Kllberg, P. (1992). Saharan dust in the Amazon basin. *Tellus B: Chemical and Physical Meteorology*, *44*(2), 133–149. https://doi.org/10.3402/tellusb.v44i2.15434

Taylor, P. A. (1977). Some numerical studies of surface boundary-layer flow above gentle topography. *Boundary-Layer Meteorology*, *11*, 439–465. https://doi.org/10.1007/BF02185870

van der Does, M., Knippertz, P., Zschenderlein, P., Harrison, R. G., & Stuut, J.-B. W. (2018). The mysterious long-range transport of giant mineral dust particles. *Science Advance*, *4*(12), eaau2768. https://doi.org/10.1126/sciadv.aau2768

Weil, J. C., Sullivan, P. P., & Moeng, C.-H. (2004). The use of large-eddy simulations in Lagrangian particle dispersion models. *Journal of the Atmospheric Sciences*, *61*(23), 2877–2887. https://doi.org/10.1175/JAS-3302.1

Weinzierl, B., Ansmann, A., Prospero, J. M., Althausen, D., Benker, N., Chouza, F., et al. (2017). The Saharan aerosol long-range transport and aerosol-cloud-interaction experiment: Overview and selected highlights. *Bulletin of the American Meteorological Society*, *98*(7), 1427–1451. https://doi.org/10.1175/BAMS-D-15-00142.1

Wilson, J. D. (2000). Trajectory models for heavy particles in atmospheric turbulence: Comparison with observations. *Journal of Applied Meteorology*, *39*(11), 1894–1912. https://doi.org/10.1175/1520-0450(2000)039⟨1894:TMFHPI⟩2.0.CO;2

Wood, N. (1995). The onset of separation in neutral, turbulent flow over hills. *Boundary-Layer Meteorology*, *76*, 137–164. https://doi.org/10.1007/BF00710894

Wu, C., Lin, Z., & Liu, X. (2020). The global dust cycle and uncertainty in CMIP5 (Coupled Model Intercomparison Project phase 5) models. *Atmospheric Chemistry and Physics*, *20*(17), 10401–10425. https://doi.org/10.5194/acp-20-10401-2020

Yu, H., Tan, Q., Chin, M., Remer, L. A., Kahn, R. A., Bian, H., et al. (2019). Estimates of African dust deposition along the trans-Atlantic transit using the decadelong record of aerosol measurements from CALIOP, MODIS, MISR, and IASI. *Journal of Geophysical Research: Atmospheres*, *124*(14), 7975–7996. https://doi.org/10.1029/2019JD030574

Zender, C. S., Bian, H., & Newman, D. (2003). Mineral dust entrainment and deposition (DEAD) model: Description and 1990s dust climatology. *Journal of Geophysical Research*, *108*(D14), 4416. https://doi.org/10.1029/2002JD002775